Corrosion Science 217 (2023) 111096

Contents lists available at ScienceDirect

Corrosion Science

journal homepage: www.elsevier.com/locate/corsci

Short communication

The correlation between the dislocation slip/grain boundary interaction mode and the resistance to SCC initiation of Alloy 690 in simulated PWR primary water

Wenjun Kuang [a,*], Zehao Ning [a], Han Yue [a], Xianchao Hao [b,*], Jiang Li [c]

[a] Center for Advancing Materials Performance from the Nanoscale (CAMP-Nano), State Key Laboratory for Mechanical Behavior of Materials, Xi'an Jiaotong University, Xi'an 710049, China
[b] CAS Key Laboratory of Nuclear Materials and Safety Assessment, Institute of Metal Research, Chinese Academy of Sciences, Shenyang 110016, China
[c] Xi'an Thermal Power Research Institute Co., Ltd, Xi'an 710032, China

ARTICLE INFO

Keywords:
Alloy
SEM
Stress corrosion
Effects of strain
Reactor conditions

ABSTRACT

Recurring step straining was applied on Alloy 690 to establish a correlation between the dislocation slip/grain boundary (GB) interaction mode and the resistance to stress corrosion crack (SCC) initiation in high temperature hydrogenated water. The intergranular carbides can suppress the dislocation transmission across GB in thermally treated Alloy 690. GBs that block dislocation slip show higher resistance to SCC initiation than those that transmit slip. Such correlation reveals that the local normal strain near GB is the primary driving force for breaching the surface oxide film over GB which is a critical prerequisite in the SCC initiation of Alloy 690.

1. Introduction

Nickel base Alloy 690 has been widely used for heat transfer tubes in pressurized water reactors (PWRs) thanks to its high resistance to stress corrosion cracking (SCC). Now an increasing number of results suggest that penetrative intergranular oxidation is a critical precursor in the SCC of many austenitic alloys in high temperature water [1–6]. The superior resistance to SCC initiation of Alloy 690 compared with other austenitic alloys like Alloy 600 is mainly due to its ability to form a protective oxide film over the random high angle grain boundary (RHAB) [7–10]. Such oxide film can protect the grain boundary from penetrative oxidation and embrittlement. Nevertheless, it has been reported that Alloy 690 is still susceptible to SCC initiation in simulated PWR primary water under dynamic straining condition [11–14] because the surface protective oxide film over grain boundary can be breached beyond repair which induces intergranular oxidation [9,15]. A SCC initiation model of Alloy 690 under dynamic straining was initially proposed by Moss et al. [8] and then substantiated by Kuang and Was [9].

According to the model proposed by Moss et al. [8], the SCC initiation of Alloy 690 comprises three stages: 1) formation of a protective oxide film over the grain boundary via fast diffusion of Cr and grain boundary migration, 2) the breach of surface oxide film under dynamic straining, and 3) intergranular oxidation occurs which finally leads to the rupture of oxidized grain boundary. Although this model is consistent with the current available experimental results, it is still very preliminary and some unresolved issues should be further addressed. For example, the breach of surface oxide film in 2nd step is a critical process in the SCC initiation of Alloy 690. How does this process occur and what is the driving force behind (strain or stress) are still not clear. Thus, it is necessary to further investigate the SCC initiation of Alloy 690 in simulated PWR primary water and improve the current model.

To clarify the fracture mechanism of the surface oxide film, it is imperative to measure the local strain state near the grain boundary. Digital image correlation (DIC) is an ideal technique for such purpose. To incorporate DIC measurement into the process of SCC initiation in harsh environment like high temperature water, we developed a recurring step straining technique which decouples the chemical and mechanical processes in SCC initiation and enables the high-resolution measurement of local strain using indigenous oxide particles as DIC markers [16]. The validity of this new technique has been confirmed as the typical microstructure features in SCC can be reproduced with it [16]. This novel technique is ideal for SCC initiation study as it enables quasi in-situ investigation on the full process.

In this work, to further improve the understanding of SCC initiation of Alloy 690 in simulated PWR primary water, this new test technique was implemented on both solution annealed (SA) and thermally treated

* Corresponding authors.
E-mail addresses: wjkuang66@gmail.com (W. Kuang), xchao@imr.ac.cn (X. Hao).

https://doi.org/10.1016/j.corsci.2023.111096
Received 14 January 2023; Received in revised form 19 February 2023; Accepted 6 March 2023
Available online 10 March 2023
0010-938X/

(TT) Alloy 690 samples. A certain number of RHABs were pre-selected and traced through the recurring step straining for each sample. After every step straining, the local strain state near each GB was measured and whether SCC initiated was checked. As such, the correlation between the local strain state and the resistance to SCC initiation can be established. The effect of intergranular carbide on the local strain distribution was also evaluated.

2. Experimental

The studied Alloy 690 plate (60.7 wt% Ni, 29.0% Cr, 9.8% Fe, 0.19% Ti, 0.03% Mn, 0.22% Al, 0.10% Si and 0.02% C) was solution annealed (1080 °C/12 min) and water quenched. Part of the solution annealed plate was further thermally treated (715 °C/15 h). Tensile samples (15 mm in gauge length and ~2.5 mm × 2 mm in cross section) were cut from the SA and TT plates respectively by electrical discharge machining (EDM). One tensile sample from each condition was tested in this work. The gauge section of each tensile sample was gradually mechanically abraded to 3000 grit, polished up to 1 μm with diamond polishing paste and finally vibration-polished with 60 nm colloidal silica suspension for 3 h. To select suitable RHABs for subsequent study, a region of interest (ROI) within the gauge section of each tensile sample was characterized with a Nordlys electron back scattering diffraction (EBSD) detector in an FEI Helios Nanolab 600 system, as shown in Fig. 1a. The EBSD pattern was collected at a step size of 1.5 μm with an electron voltage of 20 kV and a beam current of 3.4 nA. Around 40 RHABs were pre-selected from ROI for each tensile sample. The selected RHABs are nearly perpendicular to the tensile direction and the positions of those RHABs were recorded for subsequent tracking.

To decouple the effects of corrosion and straining in SCC initiation, static exposure and step straining were performed repeatedly. The tensile samples were exposed to 320 °C, 15 MPa high-purity water (containing 30 cc H_2/kg H_2O) in a refreshed autoclave system for a certain amount of time. Then the samples were taken out for step straining at room temperature. Before and after step straining, scanning electron microscope (SEM) images were taken from the pre-selected RHABs in an FEI Verios 460 microscope in secondary electron (SE) mode, as shown in Fig. 1b. Special attention was paid during the SEM imaging. The sample surface should be carefully protected from pollution, scratch or collision so as not to damage the surface oxide particles. The imaging conditions were maintained the same. To obtain high quality images for DIC analysis, the acceleration voltage and the beam current were consistently set to 10 kV and 0.4 nA respectively. The working distance was kept at 11 mm and the dwell time was set to 30 μs for high resolution. It should be noted that the magnifications of images for these two samples are different because the formed oxide particles show different sizes. The spatial resolution of DIC is dictated by the pattern size. Since the oxide particles grown on the surface of SA sample are larger than those on the TT sample, a smaller magnification was used for SA sample compared to TT sample to get a proper resolution (1500 × vs. 8000 ×). Each sample was strained to 1–1.5% at room temperature at a strain rate of 1×10^{-3}/s for each step. With the SEM images taken before and after step straining, DIC was performed to evaluate the local strain distribution near the pre-selected RHABs, as shown in Fig. 1b. The outer oxide particles formed on the sample surface were used as DIC markers as in the previous work [16]. An open-source 2D DIC software (Ncorr) was used to process those SEM images [17]. The subset radius, subset spacing, and strain radius were set to 30, 1, and 15 to achieve a balance of accuracy and efficiency. The details for each step are listed in Table 1. The total exposure time reached 2958 h and the SA and TT tensile samples were accumulatively strained to 7.4% and 6.8% respectively. There are 42 and 36 RHABs continuously tracked on SA and TT samples throughout the six steps respectively.

Given that the step height of slip band is fine (the out-of-plane strain is very small) and DIC results show negligible GB sliding, we differentiated these GBs by whether the grain boundary blocks the dislocation slips or not from the in-plane strain measurement by DIC. For TT sample, the magnification is high enough to reveal individual slip band. The GB type was determined according to the ratio (R) of the number of dislocation slip bands transmitting across GB (N_{tra}) over the number of all dislocation slip bands (N_{all}) impinging GB. A threshold value of 0.5 was used here to define the dislocation slip/GB interaction mode as in a previous work [18]. If the average of R values from the six steps was higher than 0.5, the GB was defined as GB transmitting dislocation slip (GB_T). Otherwise it was defined as GB blocking dislocation slip (GB_B). For SA sample, as the spatial resolution was insufficient to distinguish the slip bands, the slip band/GB interaction mode was determined based on the strain level near the GB. If the normal strains on both sides of the GB were high (exceeding 120% of the average strain), this GB segment was thought to possess low resistance to dislocation slip. If only one side

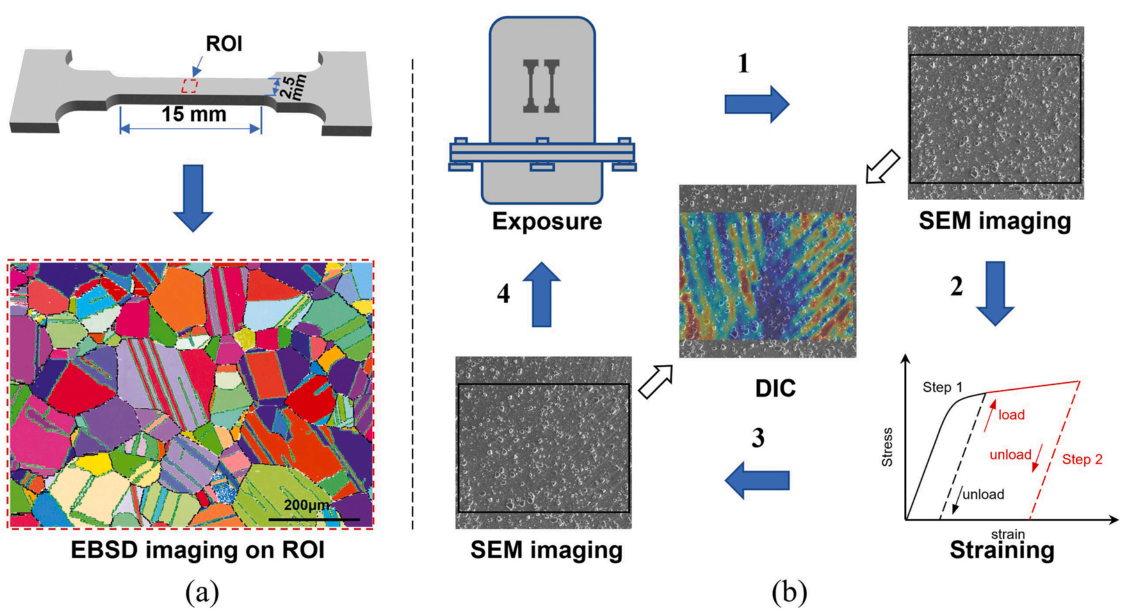

Fig. 1. (a) EBSD characterization of the ROI on the tensile sample and (b) the procedure of recurring step straining that decouples corrosion and straining (DIC was performed to evaluate the local strain distribution near GB with SEM images taken before and after step straining).

Table 1
Exposure duration and plastic strains of SA and TT tensile samples in each step.

Sample		Step 1	Step 2	Step 3	Step 4	Step 5	Step 6
SA	Exposure Duration (h)	572	523	455	438	622	348
	Plastic Strain (%)	1.07	0.98	0.85	1.50	1.51	1.48
TT	Exposure Duration (h)	572	523	455	438	622	348
	Plastic Strain (%)	0.96	0.75	0.88	1.33	1.35	1.52

of GB showed high strain level, this section was thought to block dislocation slip. The length of GB segment with low resistance to dislocation slip (L_{tra}) was measured and the GB type was determined by the ratio of L_{tra} over the total GB length (L_{all}). A threshold value of 0.5 was also used. After the step straining, every GB was examined at 8000 × to check if crack initiated and the number of cracked GBs was counted. As the intergranular carbides in TT sample is semi-continuous, some of the intergranular cracks are also semi-continuous. In this case, a

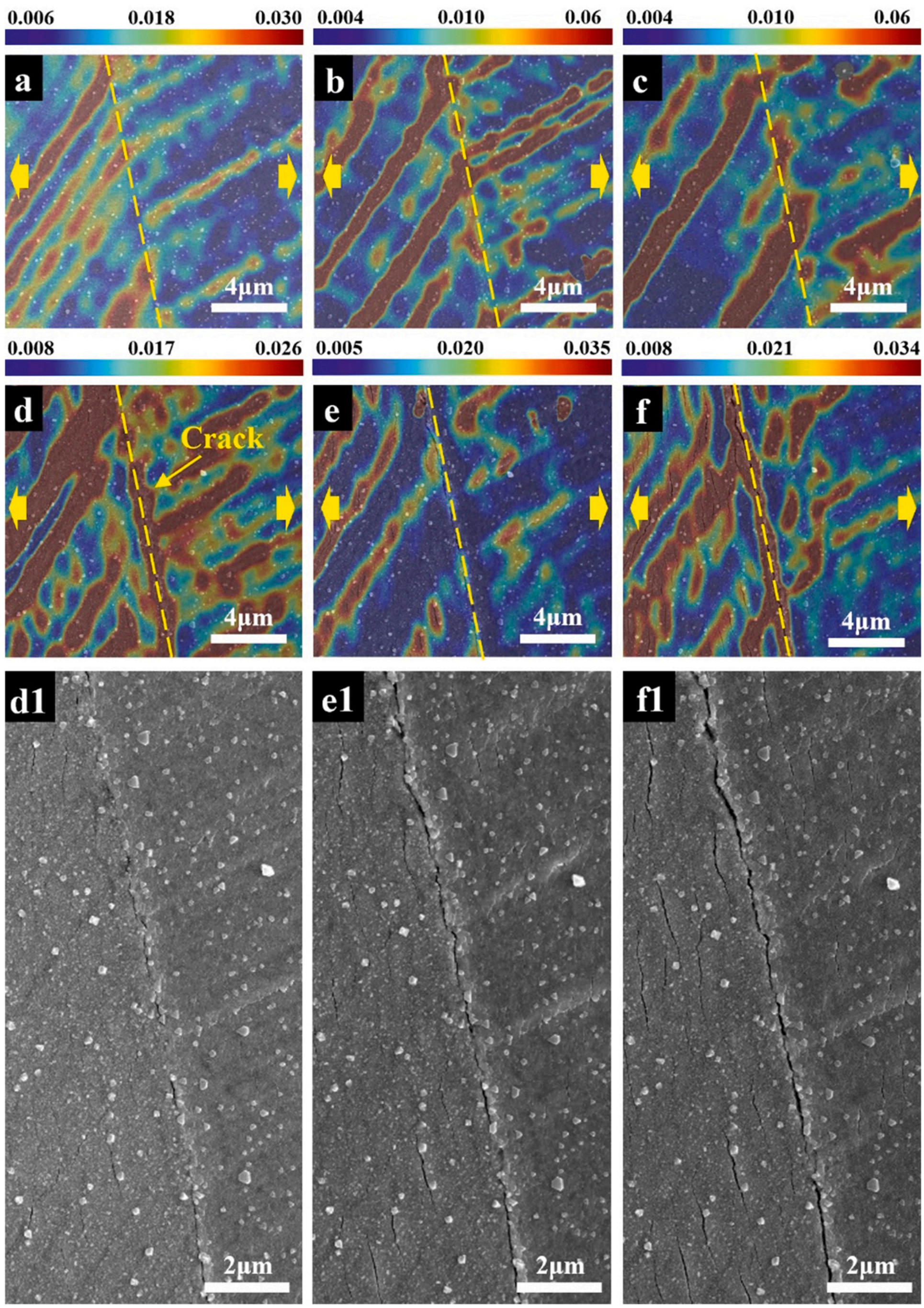

Fig. 2. (a-f) Normal strain (ε_{XX}) distribution near a grain boundary that transmits dislocation slip from the TT sample throughout the six straining steps and (d1-f1) high-magnification SEM images of the grain boundary after the last 3 straining steps.

grain boundary was counted as cracked when the length fraction of cracked section was over 50%.

3. Results and discussion

These two types of GBs show quite different strain distributions. Fig. 2a-f show the normal strain (ε_{XX}) distributions near a GB_T from the TT sample throughout the six straining steps and Fig. 2d1-f1 show the high-magnification SEM images of GB after the last 3 step strainings. The slip bands show localized high strain values and are obviously continuous across the GB from the first three steps during which crack did not initiate (Fig. 2a-c). The crack initiated during the fourth step straining which is reflected by the high strain level along the GB (Fig. 2d). The high-magnification SEM image confirms that crack initiated at this GB (Fig. 2d1). Thereafter, the linkage between the slip bands in the two grains is broken at GB (Fig. 2e and f) and the crack becomes more continuous and wider (Fig. 2e1 and f1). Nevertheless, the strain is still evenly distributed on both sides of GB. Thus, the dislocation slip/GB interaction mode has not been changed by crack initiation. The normal strain distributions near a typical GB_B from the TT sample throughout the six steps are shown in Fig. 3a-f. There are significant localized strains distributed along the slip bands on the left grain, while the right grain shows nearly no strain localization. It is then confirmed that the dislocation slip on the left grain cannot transfer across the GB. More importantly, this GB doesn't show any sign of crack initiation through the whole process, as indicated from the SEM image of GB after the last straining step (Fig. 3f1). Thus, it seems that GB_T is more susceptible to SCC initiation than GB_B for Alloy 690. Consistently, we have found that even for a single GB, the segment that transmits dislocation slip is more prone to crack initiation [16].

To establish a solid correlation between the dislocation slip/GB interaction mode and the susceptibility to crack initiation, all the pre-selected GBs were carefully analyzed. For the SA sample, 19 out of 42 GBs showed sign of blocking slip band transmission, accounting for 45.2%, as shown in Fig. 4a. Among the 36 GBs selected from the TT sample, 21 GBs block slip band transmission, accounting for 58.3%, as shown in Fig. 4b. By comparison, the proportion of GB_B on TT sample is higher than that on SA sample. That is because the carbides formed along the GBs in the TT sample can act as hindrance for dislocation movement and block the transmission of slip band across GB. Consistent phenomenon has also been reported in a previous work [14]. In the process of tracking these pre-selected GBs, it was found that the cracking resistance of GB is closely related to the dislocation slip/GB interaction mode. Fig. 4c shows the percentages of different GBs for the SA sample. For the GB_B, 17 of them didn't initiate crack while only 2 GBs cracked. So the proportion of cracked GB for this type is 10.5%. For the GB_T, 13 of them were still intact and 10 GBs cracked. The proportion of cracked GB_T is 43.5%. Thus, it seems that GB_B has higher resistance to SCC initiation than GB_T. The statistics from TT sample show a consistent trend. As shown in Fig. 4d, there are 18 uncracked GBs and 3 cracked GBs for GB_B. The proportion of cracked GB_B is 14.3%. As to GB_T, there are 8 intact GBs and 7 cracked GBs, resulting in a cracking percentage of 46.7%. This result indicates that the dislocation slip/GB interaction mode plays an important role in the SCC crack initiation of Alloy 690. SCC initiates more easily on GB that allows slip band transmission. It should be noted that from these sampled GBs, the fractions of cracked GB are comparable between these two samples. Actually, more statistically significant results (measured from a total area of ~0.5 mm^2 for each sample) show that TT sample has much lower crack length density than SA sample, confirming the mitigation effect of intergranular carbide on SCC initiation as reported before [14].

From the SCC initiation model proposed before [8], the breach of surface oxide film above GBs is a unique prerequisite for crack initiation of Alloy 690. Then it is inferred that the tendency to fracture the oxide film over GB should be directly related to the susceptibility to SCC initiation. During the dynamic straining of bulk sample, the surface oxide film would be stretched along with the substrate. Thus, the tendency to fracture the oxide film over GB should be dependent on the local strain state near GB. As the oxide film is normally brittle, it can be readily fractured when the local normal strain across GB is high. For crystalline metallic material, the plastic strain is achieved through dislocation movement. When the dislocation movement is impeded by GB which is the situation for GB_B, the local strain near GB is low (as shown in Fig. 3). In this case, the driving force for oxide film fracture is low. In contrast, when GB doesn't block the dislocation slip as in the case for GB_T (as shown in Fig. 2), the local normal strain near GB is high and the surface oxide film would be more likely to be breached. From this work, the percentage of cracked GB_T is much higher than that of GB_B for both SA and TT samples (Fig. 4), confirming that local normal strain is the primary driving force for the fracture of oxide film over GB. The

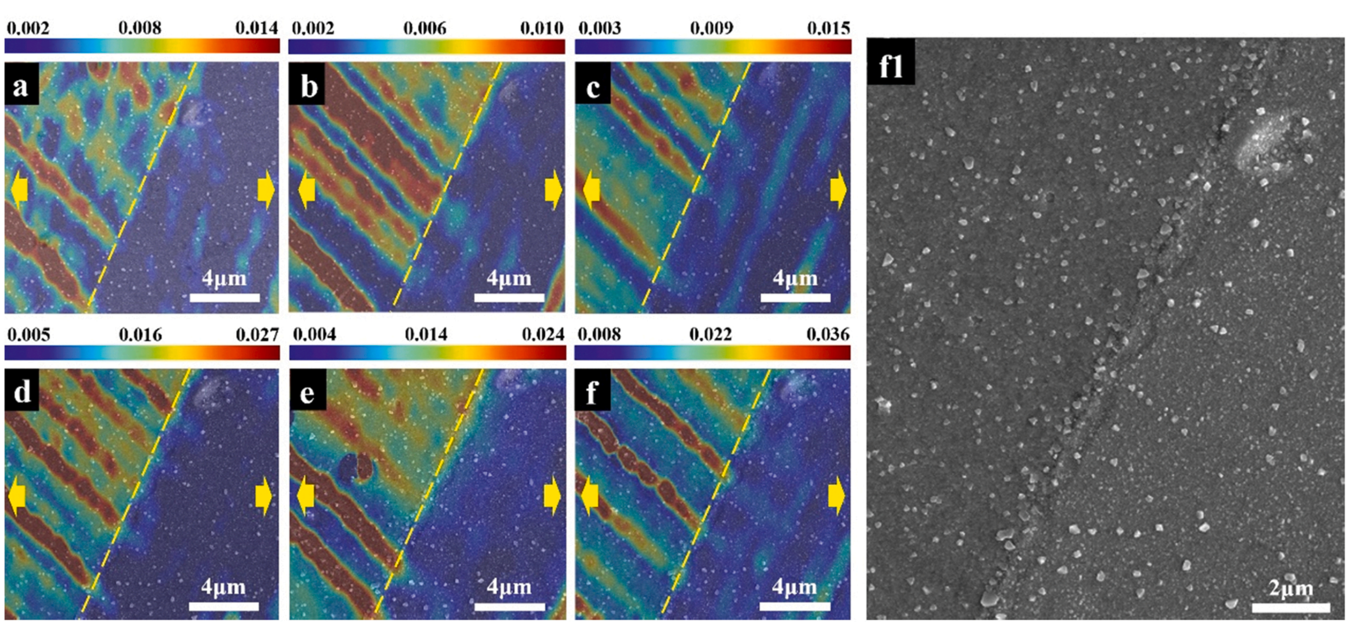

Fig. 3. (a-f) Normal strain (ε_{XX}) distribution near a grain boundary that blocks dislocation slip transfer from the TT sample throughout the six straining steps and (f1) high-magnification SEM image of the grain boundary after the last straining step.

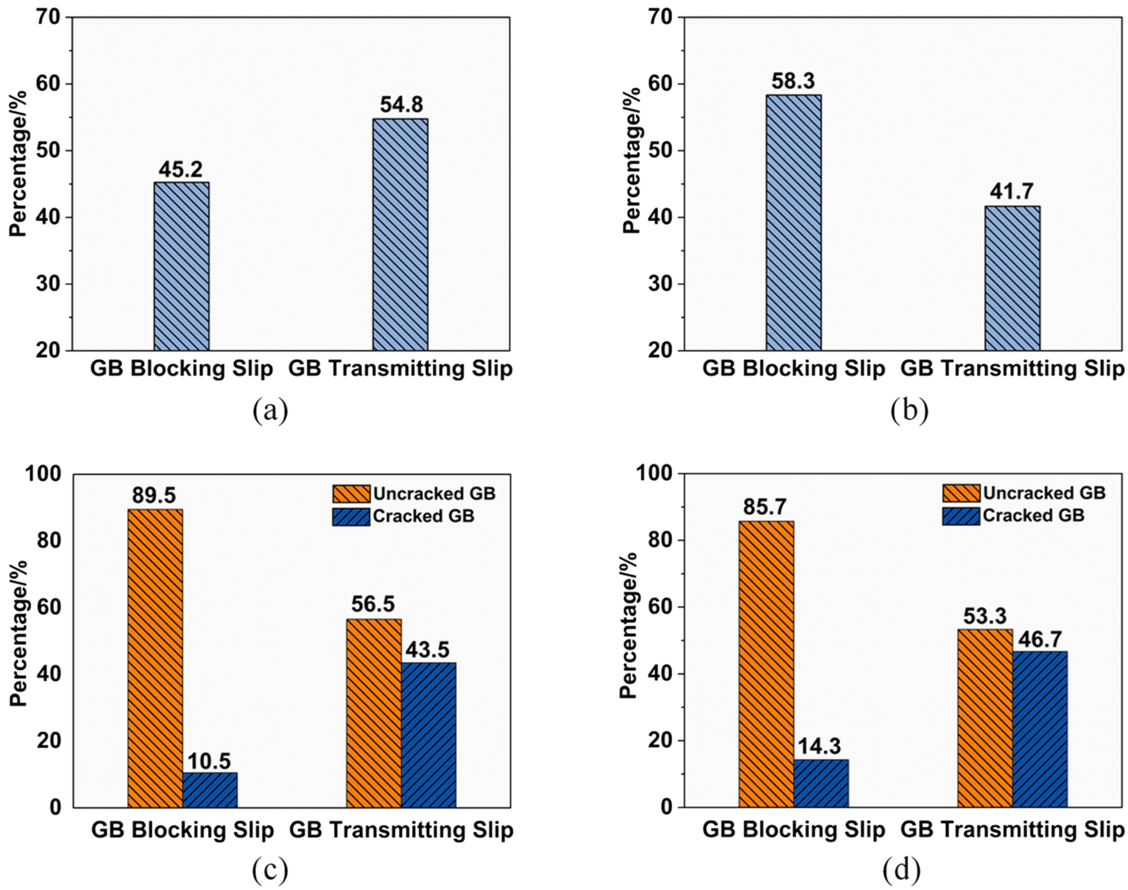

Fig. 4. The percentages of different GBs based on dislocation slip/GB interaction mode in (a) SA and (b) TT samples. The percentages of cracked and un-cracked GBs for different GB types in (c) SA and (d) TT samples.

beneficial effect of intergranular carbide in mitigating SCC of Alloy 690 can be partly attributed to its ability to impede dislocation movement across GB. Our previous work has also confirmed that the local strain near GB decorated with carbides is lower than that within the grain matrix [14].

It should be noted that the correlation between dislocation slip/GB interaction mode and the resistance to SCC initiation depends on the material studied. For materials that don't form protective oxide film over GB but tends to form intergranular oxide (like austenitic stainless steel [5,19–21]), now extensive results suggest that the SCC initiation for this type of material is driven by stress. The Schmid-Modified Grain Boundary Stress model proposed by West and Was indicates that the intergranular cracking behavior of austenitic stainless steel is strongly dependent on the local GB normal stress [22]. This model is supported by the results from irradiated 316 L stainless steel tested in supercritical water [22] and 304 stainless steel tested in high temperature oxygenated water [23]. It has also been reported that high local stress can be induced when dislocation slip is impeded by GB [24–26]. Such high stress can serve as primary driving force for crack initiation and the GB that blocks dislocation slip tends to be more susceptible to crack initiation, as reported in proton-irradiated stainless steel [27–30].

The correlation between dislocation slip/GB interaction mode and resistance to SCC initiation for Alloy 690 is summarized in Fig. 5. For GB_B (Fig. 5a-c), as the dislocation slip transmission across GB is impeded, the dislocation is accumulated near GB and the local normal strain is low. The damage to the surface oxide film formed above GB by dynamic straining is minimized and can be gradually repaired via the outward diffusion of Cr. As long as the surface oxide film over GB is intact, penetrative oxidation along GB can't occur and SCC initiation is inhibited. As for GB_T (Fig. 5d-f), the dislocation slip can transfer across GB and the normal strain near GB is nearly as large as that in the grain matrixes. In this case, the oxide film over GB can be readily breached beyond repair. Thereafter, intergranular oxidation ensues which eventually leads to crack initiation. It should be noted that only one tensile sample per heat treatment was tested in this work. It would be desirable to further confirm the observations by expanding the data volume in the future.

4. Conclusions

Recurring step straining was conducted on both solution annealed (SA) and thermally treated (TT) Alloy 690 samples exposed to high temperature hydrogenated water. The local strain distribution near pre-selected random high angle grain boundaries (RHABs) was evaluated using digital image correlation (DIC). The TT sample shows higher fraction of grain boundary (GB) that blocks slip band transmission because the intergranular carbides can hinder the movement of dislocation. For both samples, the GBs that block slip band transmission exhibit higher resistance to stress corrosion crack (SCC) initiation than those that transmit dislocation slip. That is because the breach of surface oxide film over GB is mainly driven by the local normal strain which is high when GB possesses low resistance to dislocation slip transmission.

CRediT authorship contribution statement

Wenjun Kuang: Conceptualization, Data curation, Funding acquisition, Investigation, Methodology, Project administration, Supervision. **Zehao Ning:** Data curation, Methodology. **Han Yue:** Data curation, Methodology. **Xianchao Hao:** Investigation, Funding acquisition. **Jiang Li:** Investigation, Methodology, Funding acquisition.

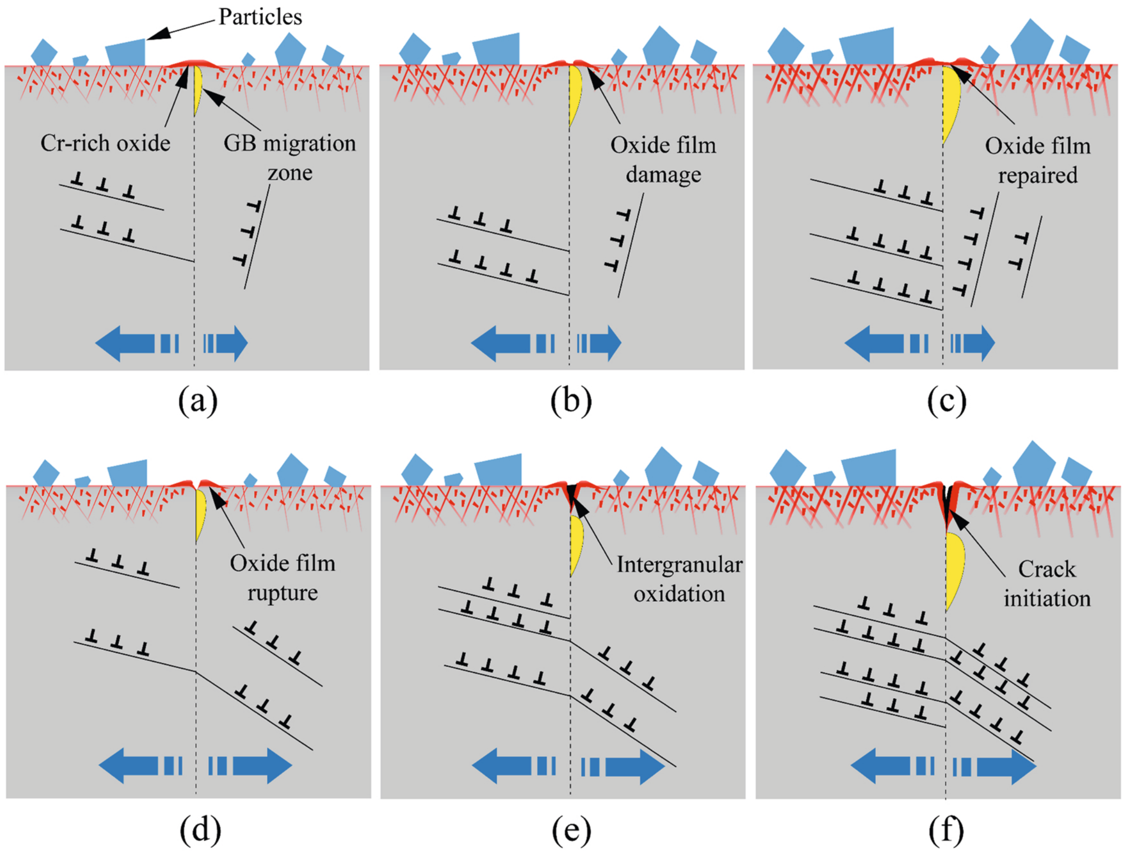

Fig. 5. Schematics of the evolution of surface oxide film over (a-c) GB that blocks dislocation slip transfer and (d-f) GB that transmits dislocation slip during dynamic straining in simulated PWR primary water.

Declaration of Competing Interest

The authors declare that they have no known competing financial interests or personal relationships that could have appeared to influence the work reported in this paper.

Data Availability

The raw/processed data required to reproduce these findings cannot be shared at this time as the data also forms part of an ongoing study.

Acknowledgements

The authors gratefully acknowledge the financial supports of National Natural Science Foundation of China (No. 51971172), Development Program of the Ministry of Science and Technology of China (No. 2019YFA0209900), open fund from CAS Key Laboratory of Nuclear Materials and Safety Assessment, Chinese Academy of Sciences (No. 2021NMSAKF02) and Shaanxi Natural Science Basic Research Program (Youth Program) (No. 2023-JC-QN-0582). The authors thank Chaowei Guo at Center for Advancing Materials Performance from the Nanoscale (CAMP-Nano) and Wei Wang at Experimental Technology Center of Xi'an Jiaotong University for their assistance with SEM analysis.

References

[1] Y.Z. Huang, J.M. Titchmarsh, TEM investigation of intergranular stress corrosion cracking for 316 stainless steel in PWR environment, Acta Mater. 54 (2006) 635–641.
[2] P.M. Scott, P. Combrade, General corrosion and stress corrosion cracking of alloy 600 in light water reactor primary coolants, J. Nucl. Mater. 524 (2019) 340–375.
[3] D. Du, K. Sun, G.S. Was, Crack initiation of neutron-irradiated 304 L stainless steel in PWR primary water, Corros. Sci. 193 (2021), 109902.
[4] D. Du, K. Sun, G.S. Was, IASCC of neutron irradiated 316 stainless steel to 125 dpa, Mater. Charact. 173 (2021), 110897.
[5] J. Xie, S. Zhang, J. Dong, S. Wang, H. Wang, W. Kuang, Insights into the superior stress corrosion cracking resistance of FeCrAl alloy in high temperature hydrogenated water: the critical role of grain boundary oxidation, Corros. Sci. 208 (2022), 110668.
[6] W. Kuang, X. Feng, D. Du, M. Song, M. Wang, G.S. Was, A high-resolution characterization of irradiation-assisted stress corrosion cracking of proton-irradiated 316L stainless steel in simulated pressurized water reactor primary water, Corros. Sci. 199 (2022), 110187.
[7] M.J. Olszta, D.K. Schreiber, M.B. Toloczko, S.M. Bruemmer, Alloy 690 surface nanostructures during exposure to PWR primary water and potential influence on stress corrosion crack initiation, in: The 16th international conference on environmental degradation of materials in nuclear power systems-water reactors, Asheville, North Carolina, USA, 2013.
[8] T. Moss, W. Kuang, G.S. Was, Stress corrosion crack initiation in Alloy 690 in high temperature water, Curr. Opin. Solid State Mater. Sci. 22 (2018) 16–25.
[9] W. Kuang, G.S. Was, A high-resolution characterization of the initiation of stress corrosion crack in Alloy 690 in simulated pressurized water reactor primary water, Corros. Sci. 163 (2020), 108243.
[10] W. Kuang, G.S. Was, The effect of grain boundary structure on the intergranular degradation behavior of solution annealed alloy 690 in high temperature, hydrogenated water, Acta Mater. 182 (2020) 120–130.
[11] T. Moss, G.S. Was, Accelerated stress corrosion crack initiation of alloys 600 and 690 in hydrogenated supercritical water, Metal. Mater. Trans. A 48 (2017) 1613–1628.
[12] W. Kuang, G.S. Was, The effects of grain boundary carbide density and strain rate on the stress corrosion cracking behavior of cold rolled Alloy 690, Corros. Sci. 97 (2015) 107–114.
[13] W. Kuang, G.S. Was, C. Miller, M. Kaufman, T. Alam, B. Gwalani, R. Banerjee, The effect of cold rolling on grain boundary structure and stress corrosion cracking susceptibility of twins in alloy 690 in simulated PWR primary water environment, Corros. Sci. 130 (2018) 126–137.
[14] W. Kuang, X. Feng, H. Yue, G.S. Was, X. Hao, Insights into the roles of intergranular carbides in the initiation of intergranular stress corrosion cracking of alloy 690 in simulated PWR primary water, Corros. Sci. 196 (2022), 110048.
[15] W. Kuang, M. Song, G.S. Was, Insights into the stress corrosion cracking of solution annealed alloy 690 in simulated pressurized water reactor primary water under dynamic straining, Acta Mater. 151 (2018) 321–333.
[16] W. Kuang, H. Yue, X. Feng, B. Yang, C. Guo, A novel test technique for the mechanistic study of initiation of environmentally assisted cracking on a

Ni–30Cr–10Fe alloy in simulated pressurized water reactor primary water, Scr. Mater. 189 (2020) 122–128.
[17] J. Blaber, B. Adair, A. Antoniou, Ncorr: open-source 2D digital image correlation matlab software, Exp. Mech. 55 (2015) 1105–1122.
[18] M.D. McMurtrey, The relation between irradiation assisted stress corrosion cracking and idslocation channeling: the role of slip interaction at the grain boundary, University of Michigan, Ann Arbor, 2014.
[19] K. Kruska, S. Lozano-Perez, D.W. Saxey, T. Terachi, T. Yamada, G.D.W. Smith, Nanoscale characterisation of grain boundary oxidation in cold-worked stainless steels, Corros. Sci. 63 (2012) 225–233.
[20] S. Wang, S. Zhang, J. Xie, X. Feng, M. Song, G.S. Was, W. Kuang, Clarifying the mitigation effect of proton irradiation on the intergranular oxidation of 316L stainless steel in high temperature water, Acta Mater. 241 (2022), 118408.
[21] P. Deng, Q. Peng, E.-H. Han, Grain boundary oxidation of proton-irradiated nuclear grade stainless steel in simulated primary water of pressurized water reactor, Sci. Rep. 11 (2021) 1371.
[22] E.A. West, G.S. Was, A model for the normal stress dependence of intergranular cracking of irradiated 316L stainless steel in supercritical water, J. Nucl. Mater. 408 (2011) 142–152.
[23] A. Stratulat, J.A. Duff, T.J. Marrow, Grain boundary structure and intergranular stress corrosion crack initiation in high temperature water of a thermally sensitised austenitic stainless steel, observed in situ, Corros. Sci. 85 (2014) 428–435.
[24] T. Benjamin Britton, A.J. Wilkinson, Stress fields and geometrically necessary dislocation density distributions near the head of a blocked slip band, Acta Mater. 60 (2012) 5773–5782.
[25] D.C. Johnson, B. Kuhr, D. Farkas, G.S. Was, Quantitative analysis of localized stresses in irradiated stainless steels using high resolution electron backscatter diffraction and molecular dynamics modeling, Scr. Mater. 116 (2016) 87–90.
[26] Y. Guo, T.B. Britton, A.J. Wilkinson, Slip band–grain boundary interactions in commercial-purity titanium, Acta Mater. 76 (2014) 1–12.
[27] D.C. Johnson, B. Kuhr, D. Farkas, G.S. Was, Quantitative linkage between the stress at dislocation channel – grain boundary interaction sites and irradiation assisted stress corrosion crack initiation, Acta Mater. 170 (2019) 166–175.
[28] M.D. McMurtrey, G.S. Was, L. Patrick, D. Farkas, Relationship between localized strain and irradiation assisted stress corrosion cracking in an austenitic alloy, Mater. Sci. Eng. A. 528 (2011) 3730–3740.
[29] M.D. McMurtrey, B. Cui, I. Robertson, D. Farkas, G.S. Was, Mechanism of dislocation channel-induced irradiation assisted stress corrosion crack initiation in austenitic stainless steel, Curr. Opin. Solid State Mater. Sci. 19 (2015) 305–314.
[30] E.A. West, G.S. Was, Strain incompatibilities and their role in intergranular cracking of irradiated 316L stainless steel, J. Nucl. Mater. 441 (2013) 623–632.